Can Photothermal Post-Operative Cancer Treatment Be Induced by Thermal Trigger?

Lei Chen[1], Qianqian Yu[1,], Kai Cheng[1], Paul D. Topham[2], Mengmeng Xu[1], Xiaoqing Sun[1], Yumin Pan[1], Yifan Jia[1], Shuo Wang[1], Linge Wang[1,]**

[1] *South China Advanced Institute for Soft Matter Science and Technology, School of Molecular Science and Engineering, Guangdong Provincial Key Laboratory of Functional and Intelligent Hybrid Materials and Devices, South China University of Technology, Guangzhou, 510640, China.*

[2] *Chemical Engineering and Applied Chemistry, School of Infrastructure and Sustainable Engineering, College of Engineering and Physical Sciences, Aston University, Birmingham, B4 7ET, UK.*

*Corresponding author: yuqianqian@scut.edu.cn, lingewang@scut.edu.cn.

ABSTRACT

One of the current challenges in the post-operative treatment of breast cancer is to develop a local therapeutic vector for preventing recurrence and metastasis. Herein, we develop a core-shell fibrous scaffold comprising of phase-change materials (PCMs) and photothermal/chemotherapy agents, as a thermal trigger for programmable-response drug release and synergistic treatment. The scaffold is obtained by *in situ* growth of a zeolitic imidazolate framework-8 (ZIF-8) shell on the surface of poly(butylene succinate)/lauric acid (PBS/LA) phase-change fibers (PCFs) to create PCF@ZIF-8. After optimizing the core-shell and phase transition behavior, gold nanorods (GNRs) and doxorubicin hydrochloride (DOX) co-loaded PCF@ZIF-8 scaffolds were shown to significantly enhance *in vitro* and *in vivo* anticancer efficacy. In a healthy tissue

microenvironment at pH 7.4, the ZIF-8 shell ensures the sustained release of DOX. If the tumor recurs, the acidic microenvironment induces the decomposition of the ZIF-8 shell. Under the second near-infrared (NIR-II) laser treatment, GNR-induced thermal not only directly destroys the relapsed tumor cells, but also accelerates DOX release by inducing the phase transition of LA. Our study sheds light on a well-designed programmable-response trigger, which provides a promising strategy for post-operative recurrence prevention of cancer.

Keywords

photothermal-chemotherapy, programmable-response, phase-change fiber, core-shell fiber, post-operative cancer recurrence, electrospinning

1. Introduction

Female breast cancer has become the most common global cancer with approximately 2.3 million new cases in 2020 alone, accounting for 11.7% of all cancer reports.[1] Surgery is the main clinical method for the treatment of primary breast cancer.[2] Despite the benefits of surgery, the post-operative recovery of patients remains unsatisfactory because of the high recurrence rate of tumors. This is mainly caused by residual tumor cells, including regeneration of the primary site and distant metastasis.[3-4] To make up for the limitations of surgical treatment, multiple therapeutic strategies have been widely used in post-operative adjuvant therapy. Among them, photothermal

therapy (PTT) [5] combined with chemotherapy has attracted significant attention to perform a synergistic effect on cancer treatment. Several nanomaterial-based systemic delivery systems that combine chemotherapies and photothermal agents have been shown to enhance drug sensitivity and overcome multidrug resistance. Examples include gold nanomaterials,[6] carbon nanomaterials,[7-8] and polydopamine (PDA) nanoparticles.[9] These systems can strongly absorb near-infrared (NIR) radiation and convert it to thermal energy to directly heat and eradicate tumor cells. SDSs triggered by the laser in the second NIR (NIR-II) biological window have a higher maximum permissible exposure (1 $W \cdot cm^{-2}$) to the skin and a deeper penetration to tumor tissue than the first NIR (NIR-I) laser, attracting widespread attention in cancer therapy.[10-11] However, as post-operative breast cancer recurrence initially starts locoregionally, local drug delivery systems are easier to meet local treatment needs due to their advantages, which include high targeting efficiency, controllable drug release and distribution, and low side effects.[12] Thus, there is urgent and critical need to develop a local therapeutic scaffold for adjuvant cancer treatment after surgery.[13]

Electrospinning, as a versatile technology to produce micro- and nanometer fibers,[14-20] is widely used in various fields, especially in tissue engineering and drug delivery.[21-25] Electrospun fibrous scaffolds have been explored to deliver photothermal-chemotherapeutic agents in a localized manner for synergistic cancer therapy.[22, 26-29] Examples include multiwalled carbon nanotubes/doxorubicin MWCNTs/DOX-co-loaded poly-L-lactic acid (PLLA) fibers,[30] DOX-loaded polypyrrole hollow fibers,[31] gold nanocage/DOX-incorporated polycaprolactone (PCL) fibers,[32] polydopamine

(PDA)-coated PCL-DOX fibers,[33] and PDA/curcumin-capped PLLA/poly(citrate siloxane) (PLLA/PCS) fibers.[13] This type of implantable scaffold based on fibers of polymers/inorganic particles/drugs increases drug accumulation that is concentrated at the lesion site, thus avoiding excessive drug circulation. However, the developed fibrous scaffolds are supposed to deliver the required high-loads of therapeutics on-demand in different tissue microenvironments before/after tumor recurrence. Therefore, the development of advanced fibrous scaffolds with controllable and programmable responsiveness is urgently sought.

Given that the local temperature can be regulated by NIR laser irradiation, one approach is to utilize thermo-responsive phase-change materials (PCMs) to prepare fibrous scaffolds. PCMs like fatty acids and alcohols can provide adjustable physicochemical parameters (e.g., mobility and density) during the phase change process.[34-36] Previous studies have demonstrated that co-loaded therapeutics can be readily released from melted PCMs by raising the temperature just above the melting point.[37-41] Thus, as fibrous PCMs, electrospun phase-change fibers (PCFs) with suitable phase-change temperature and thermo-responsive structural variation can offer a good alternative as a functional trigger in post-operative cancer treatment. The diverse compositional and thermal properties of PCFs reported pave the way for further biological applications.[42-49] In addition, to further guarantee the cyclic phase-change behavior of PCFs in a healthy tissue microenvironment and the controllable drug release in an acidic tumor microenvironment, a highly heat-resistant and acidic

microenvironment-responsive zeolitic imidazole framework-8 (ZIF-8) offers an attractive candidate as a shell wrapped around the surface of PCFs.[50]

Accordingly, in this work, we have developed a core-shell electrospun fibrous scaffold comprising of PCMs and photothermal/chemotherapy agents, as a functional trigger for programmable-response drug release and synergistic treatment. The preparation process of composite scaffolds is depicted in **Scheme 1a**. A mixture of PCM lauric acid (LA, melting point 44 °C)[51] and supporting material poly(butylene succinate) (PBS, with high melting point and good biocompatibility)[52] was electrospun into phase-change fibers (PCFs). The core-shell of ZIF-8-coated PBS/LA fibers (referred to as PCF@ZIF-8) has been optimized to obtain a scaffold with suitable phase-change temperature and stable phase-change behavior. NIR-II laser-triggered GNRs and antitumor drug DOX have been co-loaded in the optimal PCF@ZIF-8 scaffold to deliver outstanding photothermal performance and pH/thermally-triggered DOX release behavior. Subsequently, the GNR/DOX/PCF@ZIF-8 scaffolds were implanted subcutaneously in both tumor-bearing and healthy mice to evaluate the drug release behavior and antitumor effect *in vivo* (**Scheme 1b**). The GNR/DOX/PCF@ZIF-8 scaffolds implanted under the skin of healthy mice maintained a high drug concentration during treatment, indicating the potential for long-term treatment. In contrast, the same scaffold implanted inside tumor lesions showed accelerated drug release under NIR-II laser irradiation, which can effectively eliminate residual tumor cells through the synergistic effect of laser-triggered hyperthermia and programmable-response drug release. Overall, the programmable-response phase-change fibrous

scaffolds exhibit tremendous potential in adjuvant photothermal chemotherapy for post-operative cancer treatment.

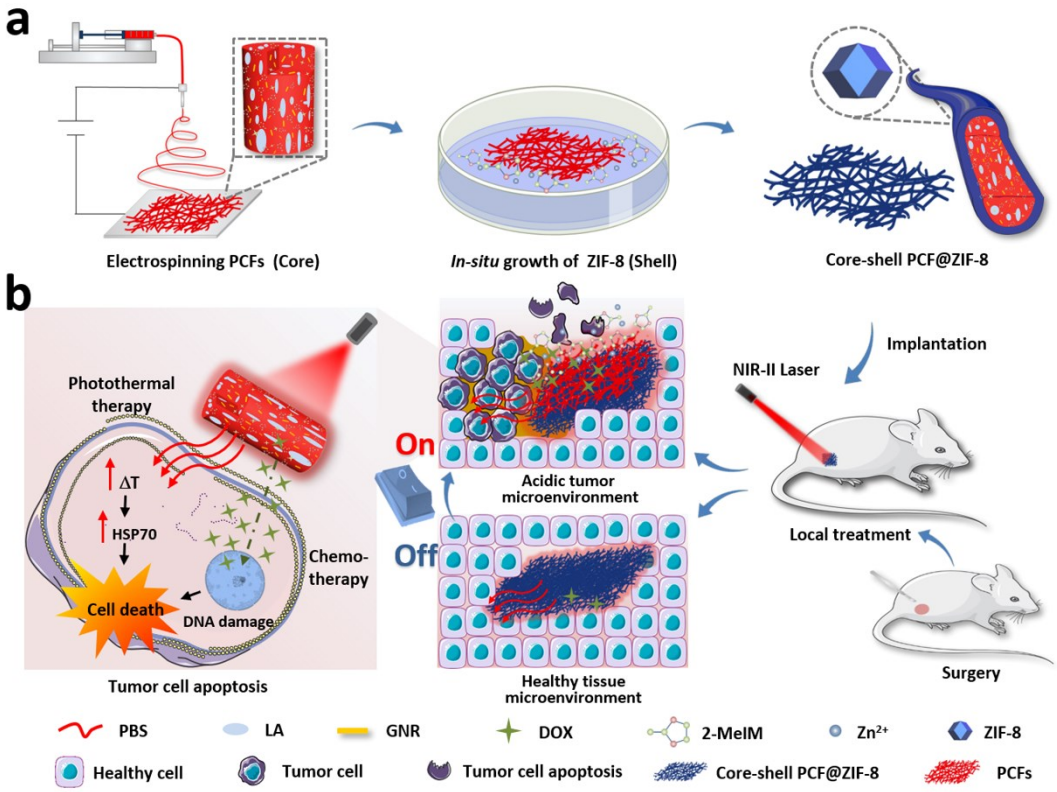

Scheme 1. Schematic diagram of the fabrication of our fibrous scaffold and *in vivo* tumor recurrence inhibition after laser treatment. (a) Preparation of the core-shell composite scaffolds loaded with GNR and DOX through electrospinning and *in situ* growth of ZIF-8. (b) Adjuvant photothermal-chemotherapy at the tumor surgical resection site for preventing recurrence of breast cancer.

2. Experimental

2.1. Materials

Poly(buttlene succinate) (PBS, M_n = 30 kDa) was purchased from Dongguan Hongli Plastic Raw Material Co., Ltd. Lauric acid (LA), doxorubicin hydrochloride (DOX), 2-methylimidazole (2-MeIM), cetyltrimethylammonium bromide (CTAB), and hydrogen tetra-chloroaurate (III) tetrahydrate ($HAuCl_4 \cdot 3H_2O$) were bought from Sigma Aldrich

(Shanghai, China). Fetal bovine serum (FBS), calcein acetoxymethyl ester (calcein-AM), phosphate buffer solution, propidium iodide (PI) and Dulbecco's modified eagle medium (DMEM) were bought from the Beyotime Institute of Biotechnology (China). Zinc nitrate hexahydrate ($Zn(NO_3)_2 \cdot 6H_2O$), sodium borohydride ($NaBH_4$), silver nitrate ($AgNO_3$), hydroquinone, and chloroform were purchased from Guangzhou Chem. Co. (Guangzhou, China). Methoxy-poly(ethylene glycol) thiol (MPEG-SH, 2000 Da) was purchased from Hua Wei Rui Ke Chemical Co. Ltd. (China). 24-well plates were purchased from NEST Biotechnology (China). Unless otherwise stated, all reagents were used as received.

2.2. Cell lines and animals

Human umbilical vein vessel endothelial cells (HUVECs) and mouse mammary tumor cell line 4T1 cells were obtained from South China University of Technology (SCUT, Guangzhou, China). All the cells were cultured in a humidified incubator (5% CO_2, 37°C). BALB/c mice (20 ± 2 g, female) were fed at 37°C and 55% humidity in the Experimental Animal Center of SCUT. All animal experiments were approved by the Institutional Animal Care and Use Committee of SCUT (AEC No. 2020048) and carried out in compliance with the protocols of the Care and Use of Laboratory Animals.

2.3. Preparation and characterization of core-shell PCF@ZIF-8 scaffolds

The core-shell PCF@ZIF-8 scaffolds were fabricated by combining uniaxial electrospinning with *in situ* growth of a shell on the fiber surface as depicted in **Scheme 1a**.[53] To explore the optimum ratio for the core, PBS and LA at different weight ratios

of 5:0, 5:3, 5:5 and 5:7 were dissolved in chloroform to prepare 20 wt% solutions for electrospinning into PCFs. Furthermore, to prepare stable and continuous core-shell fibers, 0.5 wt% 2-MeIM was mixed with the PBS/LA solution. 2-MeIM/PCFs were fabricated and soaked in a mixed solution of $Zn(NO_3)_2 \cdot 6H_2O$ and 2-MeIM for 0, 0.5, 1, and 3 minutes, respectively. The prepared PCF@ZIF-8 scaffolds were subsequently washed thrice with water and dried at 30°C.

The morphologies of the PCFs and core-shell PCF@ZIF-8 were observed by scanning electron microscopy (SEM) after gold sputter coating for 1 minute. The thermal performance and LA content of core-shell PCF@ZIF-8 scaffolds with different shell thicknesses were measured by differential scanning calorimetry (DSC) and thermogravimetric analysis (TGA), respectively. To further verify the phase transition behavior of core-shell PCF@ZIF-8 scaffolds, *in situ* time-resolved wide angle X-ray diffraction (WAXD) were carried out to detect melting and crystallization behavior of PCF@ZIF-8 scaffolds when heating from 37°C to 49°C and then cooling from 37°C to 49°C at a rate of 3°C/min.

2.4. Synthesis and characterization of GNRs

Initially, GNRs were synthesized with longitudinally localized surface plasmon resonance (LSPR) peaks in the NIR-II window. 10 mL of $HAuCl_4 \cdot 3H_2O$ (0.005 mg/mL) and 0.8 mL of 0.02 mmol/mL cold $NaBH_4$ solution were added into 10 mL of CTAB (0.1 mg/mL) solution to prepare a seed solution. After vigorous stirring (1500 rpm) for 5 minutes, the seed solution was allowed to settle for 3 h at room temperature. The

growth solution was prepared by adding 10 mL $HAuCl_4 \cdot 3H_2O$ (0.02 mg/mL) to 10 mL CTAB (0.1 mg/mL). Next, 1.2 mL $AgNO_3$ solution (0.06 mg/mL), 500 μL of hydroquinone solution (0.05 mg/mL) and 160 μL of seed solution were added consecutively by syringe to the growth solution. After allowing the solution to settle for 18 h at 30°C, GNRs were collected by centrifuging at 15000 rpm for 15 minutes. 1 mL of MPEG-SH (2 mg/mL) was added into 2 mL of as-synthesized GNR (0.4 mg/mL) solution and the mixture was further stirred at room temperature for 3 h. Finally, GNRs were collected after centrifugation at 15,000 rpm for 15 minutes. The morphology of the synthesized GNRs was observed by transmission electron microscopy (TEM), absorption spectra by UV-Vis spectroscopy (UV-Vis) and surface charge using zeta-potential.

To assess the photothermal performance of GNRs in the NIR-II window, 1064 nm laser irradiation with adjustable power density was employed. A thermal camera was used to record the temperature changes of GNR solutions (50, 150, and 300 μg/mL) that had been irradiated for 10 minutes in a quartz cell. The photothermal conversion efficiency (η) [54] of GNRs was calculated by the following equation:

$$\eta = \frac{hS\Delta T_{max} - Q_0}{I\,(1-10^{-A_\lambda})}$$

where h is the heat transfer coefficient, S is the container surface area, ΔT_{max} is the maximum temperature change of the GNRs, I is the laser power, and A_λ is the absorbance at 1064 nm. Q_0 is the heat input due to light absorption by the phosphate buffer solution. The lumped quantity hS was determined according to

$$\tau_s = \frac{Cm}{hS}$$

where C and m are the heat capacity (4.2 J/g) of water and mass (0.75 g), respectively. To obtain *hS*, θ is defined as the ratio of ΔT to ΔT_{max} *as follows*:

$$\theta = \frac{\Delta T}{\Delta T_{max}} = \frac{T - T_{surr}}{T_{max} - T_{surr}}$$

$$t = -\tau_s \ln\theta$$

2.5. Preparation and characterization of GNR/DOX co-loaded PCF@ZIF-8 scaffolds

After optimizing the PCF@ZIF-8 structure, GNRs and DOX were co-loaded into the core of the core-shell PCF@ZIF-8 scaffolds. GNRs and DOX with a concentration of ~2 wt% were firstly quantitatively calculated by inductively coupled plasma mass spectrometry (ICP-MS) and UV-Vis, and then both dissolved in the PBS/LA solution and electrospun into PCFs before *in situ* growth of the ZIF-8 shell. The morphology of the composite scaffolds was observed by SEM, energy-dispersive spectroscopy (EDS) and confocal laser scanning microscopy (CLSM). The photothermal properties of PCF@ZIF-8 and GNR/PCF@ZIF-8 scaffolds were characterized under NIR-II laser irradiation for 10 minutes. An IR thermal camera was used to record temperature changes and related thermal images of the composite scaffolds. The power density of the 1064 nm laser was varied from 0.5 $W \cdot cm^{-2}$ to 0.75 $W \cdot cm^{-2}$ and then to 1.0 $W \cdot cm^{-2}$ to irradiate phosphate buffer solutions of the GNR/PCF@ZIF-8 scaffolds. The photothermal stability of GNR/PCF@ZIF-8 scaffolds soaked in DMEM was also measured after 1, 3, and 7 days and the deep-tissue penetration of 1064 nm laser was characterized. The temperature was monitored and recorded every 30 s.

The DOX release profiles of GNR/DOX/PCF@ZIF-8 scaffolds were evaluated in a healthy tissue environment and an acidic tumor microenvironment with/without LA phase transition. 20 mg of previously obtained GNR/DOX/PCF@ZIF-8 scaffold was soaked in 5 mL phosphate buffer solutions at pH 7.4 and pH 6.0. The amount of released DOX was recorded by Spectra Max iD3 and calculated by the standard DOX curve. The accumulative released DOX was calculated using the following equation:

$$\text{Accumulative release (\%)} = \frac{w_{\text{DOX released}}}{w_{\text{total}}} \times 100\%$$

where $w_{\text{DOX released}}$ is the accumulative weight of released DOX from the GNR/DOX/PCF@ZIF-8 scaffold and w_{total} is the total weight of DOX in the GNR/DOX/PCF@ZIF-8 scaffold.

2.6. In vitro cytocompatibility assay

DMEM with 10% FBS, streptomycin and penicillin was used to culture HUVECs. The PCF@ZIF-8, GNR/PCF@ZIF-8, GNR/DOX/PCF@ZIF-8 scaffolds were placed in sterilized 24-well plates. The HUVECs with 1.0×10^4 cells per well were then cultured with scaffolds and incubated in a humidified cell incubator (5% CO_2, 37 °C) for 3 days. HUVECs were also cultured in blank wells as a control. Calcein-AM/PI was used for Live/Dead staining. To quantitatively assess the cell viability of composite scaffolds, cell counting kit-8 (CCK-8) assay was measured after 1 and 3 days. In brief, DMEM supernatant (100 μL) was collected and pipetted into a 96-well plate. The cells were incubated for 1 and 3 days, then 20 μL CCK-8 solution was added into the well for another 1.5 h. Absorbance (450 nm) was measured by Spectra Max iD3. Optical

density (OD) was recorded and cell viability was calculated using the following equation:

$$\text{Cell viability (\%)}=\frac{OD_{sample}-OD_{CCK-8}}{OD_{control}-OD_{CCK-8}}\times 100\%$$

where OD_{sample} is the absorbance of CCK-8 solution with cells and scaffolds, OD_{CCK-8} is the absorbance of CCK-8 solution without cells, and $OD_{control}$ is the absorbance of CCK-8 solution and cells without scaffolds.

2.7. In vitro antitumor efficacy

DMEM with 10% FBS, streptomycin and penicillin was also used to culture the 4T1 cells. The 4T1 cells with 2.0×10^4 cells/well were firstly seeded in 24-well plates and cultured in an incubator (37 °C, 5% CO_2). The PCF@ZIF-8, GNR/PCF@ZIF-8 and GNR/DOX/PCF@ZIF-8 scaffolds were added to the culture wells. 1064 nm laser irradiation was turned on for 10 minutes and the composite scaffolds were treated thrice. Meanwhile, as a control, 4T1 cells were also cultured without laser irradiation. Cells were stained with calcein-AM/PI for Live/Dead cell staining to observe the distribution of live and dead cells using CLSM. Then, the 4T1 cell viability was further determined by the CCK-8 assay. In Jin's method,[55] the synergetic index (Q_{A+B}) of GNR-enabled PTT and DOX-enabled chemotherapy was calculated using:

$$Q_{A+B}=\frac{E_{A+B}}{E_A+E_B-E_A\times E_B}$$

where E_A is the mortality rate of the 4T1 cells treated by PTT alone, E_B is the mortality rate of the 4T1 cells treated by chemotherapy alone, and E_{A+B} is the mortality rate of the 4T1 cells treated by the combination of photothermal-chemotherapy,

respectively. $Q_{A+B} < 0.85$ means antagonism, $0.85 \leqslant Q_{A+B} < 1.15$ means additive effects, and $Q_{A+B} \geqslant 1.15$ means synergism.

The inhibitory effect of composite scaffolds with laser treatment on the migration and invasion ability of 4T1 cells was assessed by a wound-healing-based method. To be specific, confluent 4T1 cell cultures were wounded with a 200 μL micropipette tip and immediately placed in a serum-free medium supplemented with GNR/PCF@ZIF-8+Laser, GNR/DOX/PCF@ZIF-8 and GNR/DOX/PCF@ZIF-8+Laser. Bright-field images of wounded 4T1 cell monolayers with different treatments were obtained immediately at 0 h, 12 h, 24 h, and 36 h. After obtaining three wound measurements, the extent of wound closure was quantified by ImageJ software.

2.8. In vivo antitumor efficacy

Approximately 1×10^6 4T1 cells suspended in 200 μL DMEM were inoculated subcutaneously in female BALB/c mice. When the tumor reached a size of 100 mm^3, it was excised but with a layer of the surrounding skin left to allow post-operative recurrence. Mice were randomized into 8 groups (n = 5): (G0) healthy mice implanted with a GNR/DOX/PCF@ZIF-8 scaffold; tumor-bearing mice implanted with (G1) no scaffold, (G2) PCFs, (G3) PCF@ZIF-8+Laser, (G4) GNR/PCF@ZIF-8, (G5) GNR/PCF@ZIF-8+Laser, (G6) GNR/DOX/PCF@ZIF-8, (G7) GNR/DOX/PCF@ZIF-8+Laser. The surgical sites of the mice were covered with relevant composite scaffolds according to their grouping. The size of implanted scaffold was about 0.5 × 0.8 cm. For laser treating, each mouse was treated with 1064 nm laser irradiation (0.5 $W \cdot cm^{-2}$) for

10 minutes from day 1 to day 9. An IR camera was used to monitor temperature change and record thermal images of the tumor site. The dimensions of the recurrent tumors were measured every 3 days, and relative tumor volumes calculated by the following:

$$\text{Relatively tumor volume } (\%) = \frac{L_t \times {W_t}^2}{L_0 \times {W_0}^2} \times 100\%$$

where L_t is the length and W_t is the width of the recurrent tumors on day t. L_0 is the length and W_0 is the width of the tumors on day 0.

2.9. Statistical Analysis

All experiments were performed in triplicate or more and all quantitative results were expressed as mean ± standard deviation. The statistical significance differences were determined by One-way analysis of variance (ANOVA) and Brown-Forsythe and Welch ANOVA multiple comparison tests. The differences were considered significant for P values * < 0.05, ** < 0.01 and *** < 0.001.

3. Results and discussion

3.1. Structural optimization of core-shell PCF@ZIF-8 scaffolds

To reveal the optimal composition and structure of core-shell PCF@ZIF-8 scaffolds, PCFs composed of different PBS/LA weight ratios were firstly fabricated using electrospinning. As shown in **Figure 1a**, from the images of SEM, the morphologies of the PCFs displayed cylindrical-shaped to irregular band-shaped fibers as the LA weight ratio increased from 0 wt%, 30 wt%, 50 wt% to 70 wt%, respectively. It was found that the maximum content of LA in PCFs with stable cylindrical fibrous morphology is 50

wt%. To obtain well-defined fibers with accessible phase-change behavior in all following experiments, the LA ratio was therefore fixed at 50 wt%. For achieving *in situ* growth of the ZIF-8 shell on the surface of PCFs, 0.5 wt% 2-MeIM was added into the PBS/LA solution, serving as anchor points on the surface of the PCFs.[56] The 2-MeIM/PCFs were then immersed in an aqueous solution of 2-MeIM and $Zn(NO_3)_2 \cdot 6H_2O$ as shown in **Scheme 1a**. By adjusting the soaking time, the core-shell PCF@ZIF-8 scaffolds with different shell thicknesses were obtained. As the corresponding SEM images depicted in **Figure 1b** show, 2-MeIM/PCFs without immersion in the 2-MeIM/Zn^{2+} solution possess a smooth surface. Compared with the 2-MeIM/PCFs, the rough surface of the PCF@ZIF-8 suggests that the shell composed of ZIF-8 nanocrystals grew successfully on the whole surface of the PCFs. With increasing immersion time from 0.5 minutes, then 1 minute, to 3 minutes, the ZIF-8 nanocrystals can be clearly observed from the enlarged SEM images. PCFs with different growth times for the ZIF-8 shell were named as PCF@ZIF-8_X (X represents *in situ* growth time of ZIF-8 in minutes) and their thermal performance was further characterized to optimize the core-shell fibers.

After the successful growth of the ZIF-8 shell, the LA loading within the core of the PCF@ZIF-8 fibers was determined by TGA. The PCFs degraded in two steps without overlap. The first degradation step of the prepared composite scaffold occurred in the temperature range of 30°C - 300°C, attributed to LA decomposition.[57-58] The second step occurred at 300°C - 600°C, which is related to the decomposition of PBS (**Figure S1a-b**). In the temperature range of 30°C - 600°C, there was no obvious decomposition

of the ZIF-8 nanocrystals. As shown in **Figure 1c**, the LA content in the PCFs was approximately 49.8% which is consistent with the added ratio (50 wt%). With the prolongation of ZIF-8 nanocrystals *in situ* growth time from 0.5 minutes, 1 minutes, to 3 minutes, the content of LA within the PCF@ZIF-8 decreased from 42.8%, 41.3% to 2.1%, indicating the increasing proportion of the ZIF-8 shell. The phase-change behavior of LA within the PCF@ZIF-8 fibers was measured by DSC. **Figure S1c-d** shows the DSC thermograms of pristine LA powder and PBS fibers. The melting temperatures (T_m) of LA and PBS were observed at 43.4°C and 78°C, respectively. Electrospun PCFs and core-shell PCF@ZIF-8 fibers with different ZIF-8 growth times were characterized by DSC as shown in **Figure 1d**. The T_m of LA within the PCF@ZIF-8 (42.5 – 42.6°C) is approximately the same as the T_m of pristine LA powder (43.4°C). The enthalpy of melting (ΔH_m) of LA in pristine LA, PCFs, PCF@ZIF-8_0.5, PCF@ZIF-8_1 and PCF@ZIF-8_3 was measured as 178.4 J/g, 78 J/g, 55 J/g, 37.5 J/g, and 3.5 J/g, respectively. After electrospinning and *in situ* growth of the ZIF-8 shell, there was no obvious change in the T_m of LA but ΔH_m of the PCF@ZIF-8 decreased with increasing ZIF-8 content (and concomitant decrease of LA content). Considering the solid-liquid phase transition in the fiber is required to control the drug release behavior more effectively, the *in situ* growth time of the ZIF-8 shell was fixed at 0.5 min in the remaining studies to maximize the phase change performance.

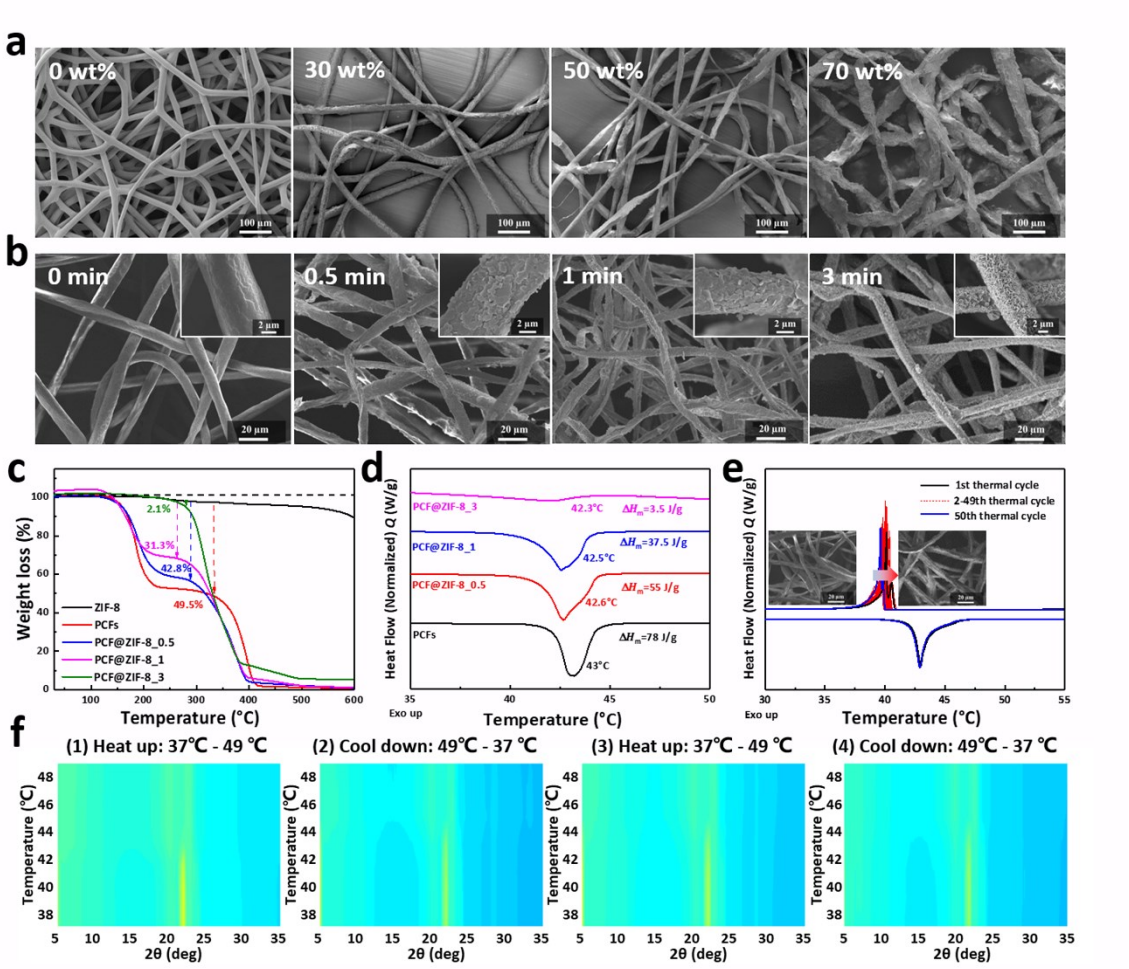

Figure 1. Structural optimization of core-shell PCF@ZIF-8 fibers. (a) SEM images of PCFs with LA weight ratios of 0 wt%, 30 wt%, 50 wt%, and 70 wt%; and (b) SEM images, (c) TGA profiles, (d) DSC thermograms of PCF@ZIF-8 with *in situ* growth time of 0 min, 0.5 min, 1 min, and 3 min. (e) DSC thermograms of PCF@ZIF-8_0.5 during 50 continuous heating-cooling cycles (with SEM image inserts before and after 50 cycles). (f) Time-resolved *in situ* WAXD data of temperature-responsive core-shell PCF@ZIF-8 fibers: where (1, 2) are the first and (3, 4) are the second heat-cooling process from 37°C to 49°C and 49°C to 37°C, respectively.

To fully probe the phase transition of LA and thermal stability of the optimized core-shell PCF@ZIF-8, PCF@ZIF-8_0.5 scaffolds were tested by continuous cyclic heating and cooling processes in the temperature range of PTT.[48] **Figure 1e** shows the DSC thermograms of a representative sample during 50 continuous heating-cooling cycles. During the cycles, the T_m and crystallization temperature (T_c) were consistently around

43°C and 40°C, respectively, which are in the range of the human body (37°C) to PTT temperatures (48°C).[59-60] The ΔH_m and enthalpy of crystallization (ΔH_c) were 55 J/g and 54.6 J/g respectively, which remained in 50 cycles. By SEM observation, there was no obvious change in fiber morphology, and no leakage of LA was found from the fibers, confirming the high thermal stability of the PCF@ZIF-8 scaffolds attributed to the protection of the heat-resistant ZIF-8 shell. Meanwhile, time-resolved *in situ* WAXD was conducted to further verify the phase-change behavior of LA within the PCF@ZIF-8 scaffold. The thermal-profile of the WAXD experiment was increased from 37°C to 49°C at 3°C/min, isothermal for 5 minutes, and then decreased from 49°C to 37°C at 3°C/min, which is in line with the temperature profile of clinical PTT. **Figure 1f** shows the phase transition process of LA in two cycles of heating and cooling treatment. From the integrated WAXD files, the characteristic peak of LA ($2\theta = 21.7°$) is observed from 37°C to 49°C, which indicates the high crystallinity of LA in PCF@ZIF-8 scaffolds.[57] When the temperature exceeds 43°C, the crystallization peak of LA gradually disappears, indicating that the LA solid-liquid phase transition has occurred. After being isothermal for 5 min, the cooling procedure was executed. The crystallization peak of LA gradually appeared and became stronger when the temperature dropped below 43°C. The same phenomena were also observed in the second heating-cooling cycle, which strongly demonstrates the cyclic phase-change capability of our PCF@ZIF-8 scaffold.

3.2. Morphology of GNRs and GNR/DOX co-loaded PCF@ZIF-8 scaffolds

GNRs for PTT in the NIR-II window were synthesized following the previous a seed-mediated method.[61-62] The zeta potential of CTAB-coated GNR was highly positive (30.25 ± 0.76 mV), whereas that of PEG-coated GNR reduced to 4.1 ± 0.45 mV (Figure S2a). The decrease in zeta potential confirms that mPEG-SH replaced the CTAB layer successfully. As shown in Figure 2a, the morphology of the GNRs was characterized by TEM and the aspect ratio was calculated by ImageJ software. The dimensions of the GNRs were found to be 91.53 ± 18.56 nm and 10.69 ± 1.57 nm. The aspect ratio of the GNRs was approximately 8:1 and displayed two characteristic peaks including a longitudinal LSPR peak around 1034 nm and transverse LSPR peak around 510 nm, as shown in **Figure 2b**, suggesting their potential photothermal conversion capability in the NIR-II window. The photothermal conversion properties were preliminarily evaluated using a 1064 nm laser device and a real-time infrared thermal camera. The recorded infrared thermal images and heating curves of GNRs are shown in **Figure S2b** and **Figure 2c**. With increasing concentration of GNRs (50 μg/mL, 150 μg/mL, 300 μg/mL), the temperature of the solutions gradually increased to 40.6°C, 49.5°C and 74.4°C, respectively upon NIR-II irradiation (1 $W \cdot cm^{-2}$), whereas there was no obvious increase in the temperature of the control (phosphate buffer solution). A similar result was also observed upon NIR-II irradiation with different power density. The temperature of the GNR solution (300 μg/mL) increased to 44.4°C, 57.3°C, and 74°C for 0.5 $W \cdot cm^{-2}$, 0.75 $W \cdot cm^{-2}$, 1 $W \cdot cm^{-2}$, respectively (**Figure S2c-e**). The temperature of the GNR solution displayed no noticeable change after undergoing three irradiation

cycles, indicating excellent photothermal stability. The photothermal conversion efficiency (η) of the prepared GNRs was further calculated (according to previous reports) to be 34.2%, which was higher than NIR-I laser-triggered GNRs.[54, 63-64] The above results indicated the successful synthesis and excellent photothermal performance of GNRs.

The GNR and DOX co-loaded PCF@ZIF-8 scaffold was further prepared according to the optimization process. 2 mg GNRs (the concentration of gold ions: 649.4187 mg/L) and 1.945 mg DOX quantitatively calculated by ICP-MS and UV-Vis were loaded within PCF@ZIF-8 scaffold (**Figure S3a**). SEM images shown in **Figure 2d-e** reveal the morphology of GNR/DOX/2-MeIM/PCFs and GNR/DOX/PCF@ZIF-8 scaffolds. GNR/DOX/2-MeIM/PCFs still show a uniform smooth and knotless morphology. After *in situ* growth of the ZIF-8 shell, the surface of the GNR/DOX/PCF@ZIF-8 scaffold became rough (**Figure 2e1**). Elemental mapping detected by EDS shows that the C, N, Au elements and C, N, Au, Zn elements were uniformly distributed in GNR/DOX/2-MeIM/PCFs and GNRs/DOX/PCF@ZIF-8 scaffolds, respectively, confirming both the loading of GNRs and the growth of ZIF-8 nanocrystals (**Figure 2d2 and e2**). Considering that the anticancer drug DOX exhibits inherent red fluorescence, CLSM was used to verify the DOX loading within the composite scaffolds. Red fluorescence can be seen distributed along the fibers before and after ZIF-8 growth in the CLSM images (**Figure 2d3 and e3**), showing that DOX can be encapsulated into the composite scaffolds. The X-ray diffraction (XRD) patterns showed the crystallization peaks of PBS (2θ = 19.4° and 22.5°), LA (2θ = 21.7° and 24.3°), ZIF-8 (2θ = 7.2° and 10.4°) in

the composite scaffolds (2θ = 7.3°, 10.4°, 19.4°, 21.7°, 22.5°, and 24.3°), indicating the presence of the crystalline forms of the different components within the GNR/DOX/PCF@ZIF-8 scaffold (**Figure S3b**). Together, these results demonstrate that GNR and DOX co-loaded PCF@ZIF-8 scaffolds can be successfully fabricated by electrospinning and post-treatment.

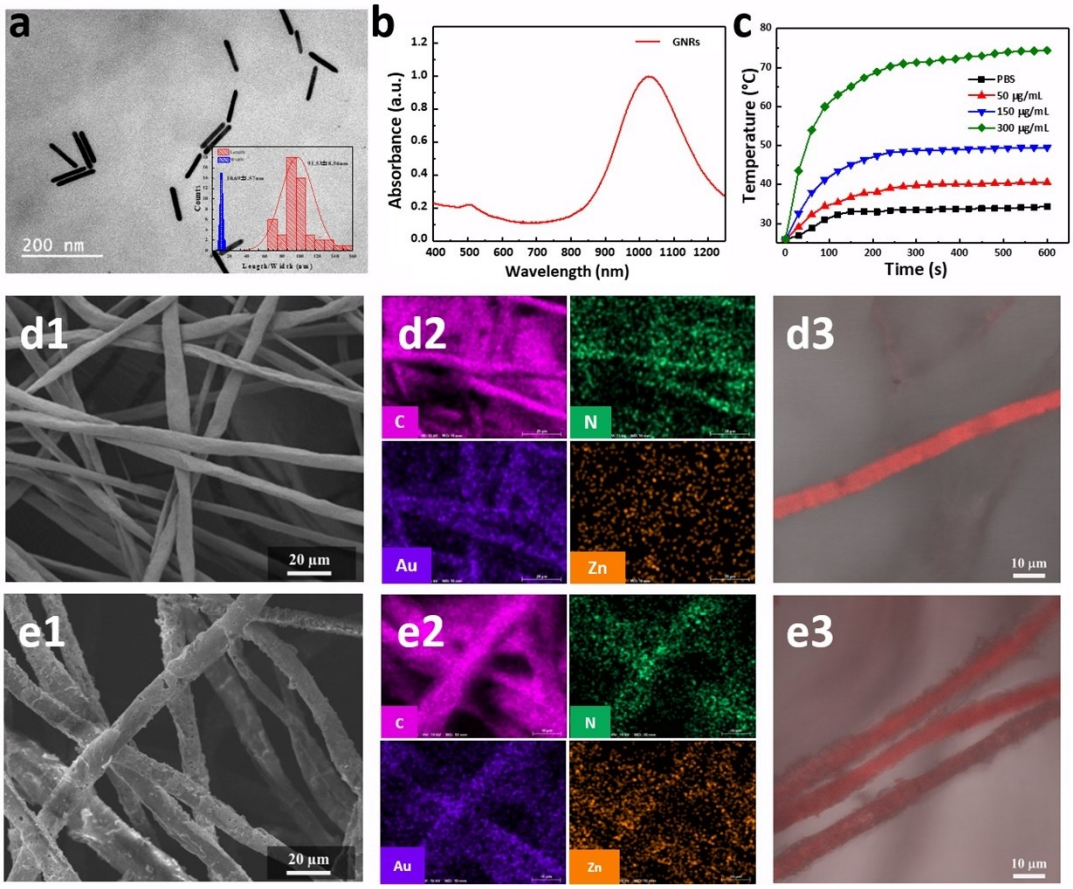

Figure 2. Morphology and photothermal performance of GNRs and morphology of GNR/DOX co-loaded PCF@ZIF-8 scaffolds. (a) TEM images of synthesized GNRs and statistical length and diameter. (b) UV-Vis spectrum of the GNRs. (c) Temperature change in GNR solutions at different concentrations under NIR-II laser irradiation. (d1, d2, d3) SEM images, corresponding EDS elemental mapping, and CLSM images of GNR/DOX/2-MeIM/PCFs. (e1, e2, e3) SEM images, corresponding EDS elemental mapping, and CLSM images of GNR/DOX/PCF@ZIF-8 scaffolds.

3.3. Photothermal performance of composite scaffolds

To assess the photothermal performance, the temperature changes of the GNR/PCF@ZIF-8 scaffold under constant NIR-II laser irradiation was monitored in real-time by an infrared thermal camera. The infrared thermal images and the corresponding heating curves of the temperature changes of GNR/PCF@ZIF-8 scaffolds treated with 1064 nm laser irradiation with different power densities for 10 minutes are depicted in **Figure 3a and Figure S4a**. As the power density was increased (0.5 $W \cdot cm^{-2}$, 0.75 $W \cdot cm^{-2}$, and 1 $W \cdot cm^{-2}$), the temperature increased to 44.3°C, 51.7°C, and 64.2°C, respectively, indicating a significant laser power density-dependent temperature increase, whereas no obvious changes were observed on the 0.5 $W \cdot cm^{-2}$ laser-irradiated PCF@ZIF-8 scaffolds (**Figure 3b**). The stability of photothermal conversion performance of the GNR/PCF@ZIF-8 scaffold was characterized after immersion in DMEM for 1, 3, and 7 days. The temperature of DMEM remained stable (~45°C) under laser irradiation at 0.5 $W \cdot cm^{-2}$ (**Figure 3c**). Clearly, our results show that the temperature of the composite scaffold can be raised to more than 43°C using 1064 nm laser irradiation, which is high enough to kill tumor cells by hyperthermia, as reported previously.[5] The NIR-II window can offer higher tissue-penetration depth than the commonly explored NIR-I window and therefore we further evaluated the tissue-penetration performance in the NIR-II window.[65] To simulate the deep-tissue condition for PTT *in vivo*, pork tissues of various thickness (0, 3, 6 and 9 mm) were placed on the top of the scaffold and then irradiated at 1064 nm (1 $W \cdot cm^{-2}$, 10 minutes). The maximun temperature changes (ΔT) of composite scaffolds under these different conditions

reached approximately 40.7°C, 20.1°C, 13.8°C, and 9.6°C, respectively (**Figure S4b**). These results demonstrate that the GNR/PCF@ZIF-8 scaffold possesses excellent photothermal conversion efficiency, photothermal stability, and high tissue penetration for local PTT.

3.4. In vitro drug release

It is well known that the tumor microenvironment is slightly more acidic than healthy tissue.[66] And, on account of the photothermal-triggered phase transition of LA, the DOX release behavior from the composite scaffolds was further evaluated upon pH and temperature variation. To mimic the slightly acidic environment of tumor tissue and that of healthy tissue, phosphate-buffer solution at pH 6.0 and 7.4 was used as the release medium, respectively. As shown in **Figure 3d**, under different conditions, the amount of DOX released from the GNR/DOX/PCF@ZIF-8 scaffold increased with time. For the non-irradiated group, at pH 7.4, approximately 10 ± 0.37% DOX was released within 21 days, while 15.9 ± 0.75% was released in the same period at pH 6.0. This phenomenon may be attributed to the decomposition of the ZIF-8 shell, which can increase the contact area between the composite PCFs and phosphate buffer solution. Before sampling at each time point, the scaffold immersed in phosphate buffer solution at pH 6.0 was irradiated for 10 minutes. For the NIR-II laser-irradiated group, at pH 6.0, approximately 26 ± 2.29% DOX was released within 21 days, which is attributed to the solid-to-liquid phase transition of LA caused by the temperature variation. As shown in the drug release profile, a relatively rapid drug release rate was realized under

acidic microenvironment and laser irradiation, indicating the controllability of drug release behavior.

To further explore the mechanism of drug release behavior affected by the variation of pH value and temperature, the morphological and structural changes of the composite scaffolds under different conditions were observed by SEM. From the SEM images in **Figure 3e (1)**, the core-shell of the GNR/DOX/PCF@ZIF-8 scaffold soaked in phosphate buffer solution at pH 7.4 was almost unchanged after 1, 3, 5, and 7 days. However, when composite scaffolds were soaked in phosphate buffer solution at pH 6.0, the decomposition of the ZIF-8 shell began to occur on the surface of PCFs at 5 minutes, and the degree of ZIF-8 decomposition gradually increased with time, with the ZIF-8 shell completely disappearing by 30 minutes. Elemental mapping detected by EDS shows that the Zn element distributed in the scaffold gradually disappeared with time, confirming the decomposition of ZIF-8 (**Figure S4c**). The dissolution of ZIF-8 is due to nitrogen protonation of the imidazole ligand under acidic conditions.[67] Additionally, after soaking in phosphate buffer solution at pH 6.0, the PCFs were gradually deformed or fractured with the increase of laser irradiation time due to the phase-change behavior of LA that occurred within the GNR/DOX/PCF@ZIF-8 scaffold (**Figure 3e (2)**). Thus, the sustained drug release of core-shell GNR/DOX/PCF@ZIF-8 scaffolds under healthy tissue conditions primarily occurs by diffusion of drug molecules through the pores of the ZIF-8 shell. The rapid drug release of the composite scaffolds under acidic conditions is mainly attributed to the diffusion of drug molecules from the molten LA core without the limitation of the ZIF-8 shell.

The pH and photothermal-response GNR/DOX/PCF@ZIF-8 scaffolds can effectively regulate the drug release behavior, which is of significance in chemotherapy processes, particularly in long-term localized cancer treatment.

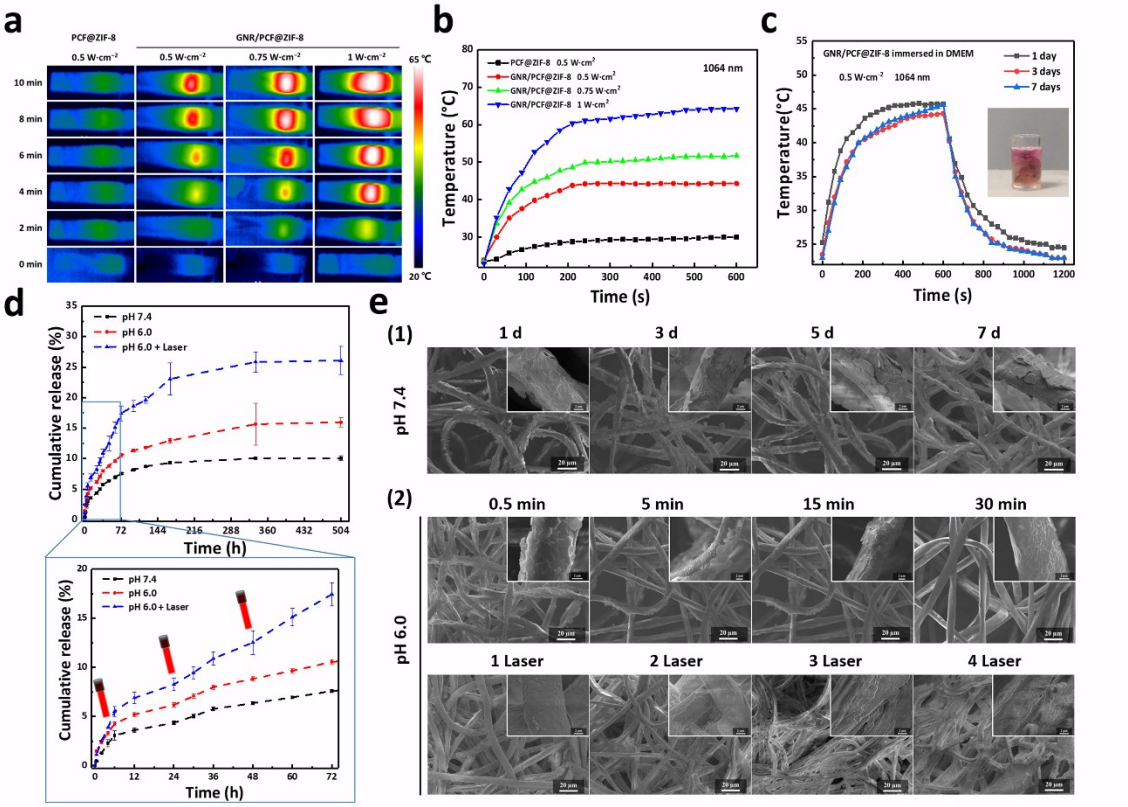

Figure 3. Photothermal performance and drug release behavior of GNR/DOX co-loaded PCF@ZIF-8 scaffold. (a, b) The infrared thermal images and heating curves of PCF@ZIF-8 and GNR/PCF@ZIF-8 scaffolds immersed in aqueous solution at different laser power densities. (c) Heating curves of GNR/PCF@ZIF-8 scaffolds immersed in DMEM after 1, 3, and 7 days. (d) pH/NIR-II laser-triggered release of DOX from GNR/DOX/PCF@ZIF-8 scaffolds. (e) SEM images: GNR/DOX/PCF@ZIF-8 scaffolds incubated in (1) phosphate buffer solution (pH 7.4) after 1, 3, 5, and 7 days without laser irradiation. (2) phosphate buffer solution (pH 6.0) after 0.5, 5, 15 and 30 minutes without laser irradiation and phosphate buffer solution (pH 6.0) after laser irradiation (0.5 W·cm^{-2}) of 1, 2, 3 and 4 times. (n = 3).

3.5. In vitro biocompatibility assay

Before *in vitro* and *in vivo* antitumor experiments, the biocompatibility of the composite scaffolds was evaluated. HUVECs were seeded on 96-well plates with

PCF@ZIF-8, GNR/PCF@ZIF-8, and GNR/DOX/PCF@ZIF-8 scaffolds for 1 and 3 days. From the fluorescent images shown in **Figure S5a**, there was no clear observation of PI stained HUVECs, indicating that composite scaffolds had low toxicity for normal cells. Cell viability and cell proliferation were quantitatively examined by CCK-8 assay (**Figure S5b, c**). The results showed that HUVECs had good survival rate and clear cell proliferation, the viability of HUVECs remained over 85% when cultured with various scaffolds, suggesting that these scaffolds have good biocompatibility. The photothermal cytotoxicity of PCF@ZIF-8, GNR/PCF@ZIF-8 and GNR/DOX/PCF@ZIF-8 scaffolds was investigated when laser irradiation was applied for 10 minutes.

In the Live/Dead staining images of **Figure 4a**, the HUVECs treated with different scaffolds showed barely any dead HUVECs with laser power density at 0.5 $W \cdot cm^{-2}$ and 0.75 $W \cdot cm^{-2}$. However, a mass of dead HUVECs appeared when the laser power density increased up to 1 $W \cdot cm^{-2}$, which was mainly attributed to the excessive heat generated by the GNRs. The quantitative data examined by the CCK-8 assay (**Figure 4b**) also demonstrated that excessive temperatures can cause cell death, indicating the photothermal treatment should be kept within a suitable temperature range.

3.6. In vitro antitumor assay

After verifying the biocompatibility, we further explored the antitumor effect of the composite scaffolds *in vitro*.[68] 4T1 cells were treated with PCF@ZIF-8, GNR/PCF@ZIF-8, and GNR/DOX/PCF@ZIF-8 scaffolds with and without laser

treatment. The cell viability of treated 4T1 cells was characterized by Live/Dead staining and the CCK-8 assay. Primarily, the cell apoptosis after 1064 nm laser irradiation with different power densities was investigated. The CLSM images of Live/Dead staining in **Figure S6a** showed that few dead cells were observed without laser irradiation (0 $W \cdot cm^{-2}$), while a great number of dead cells appeared after laser treatment (0.5, 0.75 and 1 $W \cdot cm^{-2}$) for 10 minutes. The results in **Figure S6b** showed that the cell viability of the 4T1 cells treated with PCF@ZIF-8, GNRs/PCF@ZIF-8, and GNRs/DOX/PCF@ZIF-8 scaffolds without irradiation were ~93.4%, ~85.8%, and ~83.6%, respectively, suggesting that a single scaffold without laser irradiation has insufficient ability to kill tumor cells. When the applied laser power density was 0.5 $W \cdot cm^{-2}$, 0.75 $W \cdot cm^{-2}$, and 1 $W \cdot cm^{-2}$ (1064 nm, 10 minutes, one time), the cell viability for the GNR/DOX/PCF@ZIF-8 scaffold significantly decreased to ~70.7%, ~60.8%, and ~36.8%, while that for the PCF@ZIF-8 scaffold was ~95.4%, ~95.7%, and ~92.8% and the GNR/PCF@ZIF-8 scaffold was ~77.2%, ~72.1%, and ~43.2%, respectively. The results provide further evidence that the released DOX and hyperthermia triggered by the laser-irradiated GNR/DOX/PCF@ZIF-8 scaffold led to the lowest tumor cell viability among all groups, confirming a significantly synergetic effect of photothermal and chemotherapy *in vitro*.

To further investigate the irradiation time on the viability of 4T1 cells, the composite scaffolds were irradiated (1064 nm, 0.5 $W \cdot cm^{-2}$, 10 minutes) for 0, 1, 2, and 3 times (**Figure 4c**). After irradiation, the cell viability for the GNR/DOX/PCF@ZIF-8 scaffold significantly decreased to ~73.5%, ~47.3%, and ~17.6%, while that for the PCF@ZIF-

8 group was ~87.4%, ~86.3%, and ~85.6% and the GNR/PCF@ZIF-8 scaffold was ~76.1%, ~65.8%, and ~50.3%, respectively. The CLSM images of Live/Dead staining (**Figure 4d**) also showed that the amount of living 4T1 cells (green) gradually decreased with increasing irradiation time. Compared with PCF@ZIF-8 and GNR/PCF@ZIF-8, GNR/DOX/PCF@ZIF-8 scaffolds showed higher cell killing efficiency. The synergistic index (QA+B) was calculated using the mortality rate of the treated 4T1 cells (16.4% for GNR/DOX/PCF@ZIF-8, 49.7% for GNR/PCF@ZIF-8+Laser, and 82.4% for GNR/DOX/PCF@ZIF-8+Laser).[55] In our study, the synergistic index (QA+B) was 1.42, showing a synergistic effect (QA+B > 1.15) of photothermal and chemotherapy. These results clearly demonstrate the excellent photothermal-chemotherapeutic efficiency of the GNR/DOX/PCF@ZIF-8 scaffold *in vitro*. Considering the balance of photothermal cytotoxicity to tumor cells and normal tissue cells, the laser density of 0.5 $W \cdot cm^{-2}$ was fixed in the following *in vitro* and *in vivo* experiments.

The migration of tumor cells plays an important role in several processes of tumor development, such as new angiogenesis and metastasis.[4] A wound healing test provides an opportunity to observe the inhibition of 4T1 cell migration by our composite scaffolds *in vitro*. As shown in **Figure 4e**, after scratch test treatment, the very dense 4T1 cells in the control gradually grew into the interspace of the wound with time and cells migrated to 73% of the wound healing after 36 h of serum-free culture, while cells treated by GNR/DOX/PCF@ZIF-8 and GNRs/PCF@ZIF-8+Laser scaffolds rarely moved into the interspace of the wound and cell migration rates reached 20% and -5%

at 36 h, respectively (**Figure 4f, g**). Cells treated by GNR/DOX/PCF@ZIF-8+Laser scaffolds also failed to grow into the wound area and the cell density decreased remarkably due to cell apoptosis, suggesting that GNR/DOX/PCF@ZIF-8+Laser scaffolds significantly inhibit cell migration.

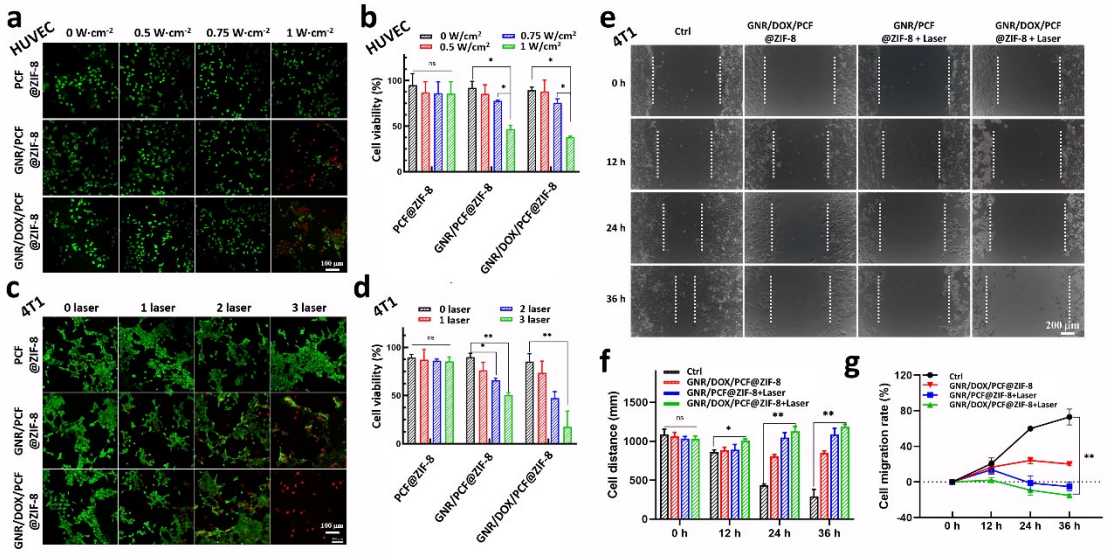

Figure 4. *In vitro* cell viability of treated HUVEC and 4T1 cells. (a, b) Live/Dead staining images and cell viability of HUVECs following treatment with different scaffolds under 1064 nm laser irradiation with different power densities. (c, d) Live/Dead staining and cell viability of 4T1 cells following treatment with different scaffolds under laser irradiation (0.5 W·cm^{-2}) at different times. (e) Cell migration ability observed by optical microscopy after different treatments using a wound-healing assay. (f) Statistical analyses on the average spacing of cell patterns over different cell-culture periods. (g) Cell migration rates of 4T1 cells after different treatments over different incubation periods. (n = 3).

3.7. In vivo photothermal imaging and fluorescence/magnetic resonance imaging

The treatment schedule of surgical tumor reduction and *in vivo* imaging is shown in **Figure 5a**. The laser treatment groups were irradiated by 1064 nm laser (0.5 W·cm^{-2}, 10 min) every two days at the beginning of treatment. To verify the *in vivo* photothermal

effect of the composite scaffolds, we monitored the temperature changes on the 4T1 tumor-bearing mice by an infrared thermal camera in real-time. As depicted in **Figure 5b**, **c**, after irradiation, the recorded temperature at the location of the tumor site in G3 was not significantly elevated, confirming that 1064 nm laser irradiation alone could not generate adequate heat without a photothermal agent. For G5 and G7, the temperature at the tumor site gradually increased to 47°C with prolonged irradiation time, suggesting that GNR/PCF@ZIF-8 scaffolds can strongly absorb NIR-II laser and convert it to thermal energy *in vivo*.

The feasibility of monitoring the implanted composite scaffolds and guiding remote photothermal-chemotherapy was evaluated by *in vivo* fluorescence/magnetic resonance (FL/MR) imaging. Taking advantage of the strong inherent fluorescence of DOX loaded in the PCF@ZIF-8 fibers, the GNR/DOX/PCF@ZIF-8 scaffold was implanted under the skin of healthy mice (G0) and into the tumor resection bed of 4T1 tumor-bearing mice (G7) and then imaged via *in vivo* FL imaging system. The fluorescence signals were detected at four time points during the treatment period (1, 7, 14 and 21 days). As shown in **Figure 5d**, **e**, it can be found that the fluorescence intensity of G0 remained unchanged, while the fluorescence intensity of G7 decreased with time and distributed around the tumor site after periodic laser irradiation, indicating the pH/photothermal-triggered DOX release. The T1-weighted and T2-weighted MR imaging acquired using a 3.0T MRI scanner at three time points (5, 10 and 20 days) showed the different tumor recurrence of G1 and G7 samples at the cross-section of the tumor site (**Figure 5f**). There were no significant solid tumors of G7 during the

treatment, while the solid tumors of G1 were growing with time and almost became life-threatening. *In vivo* FL and MR imaging delineates the status of implanted scaffold and facilitates comprehensive diagnosis of the tumor recurrences during post-operative treatment.

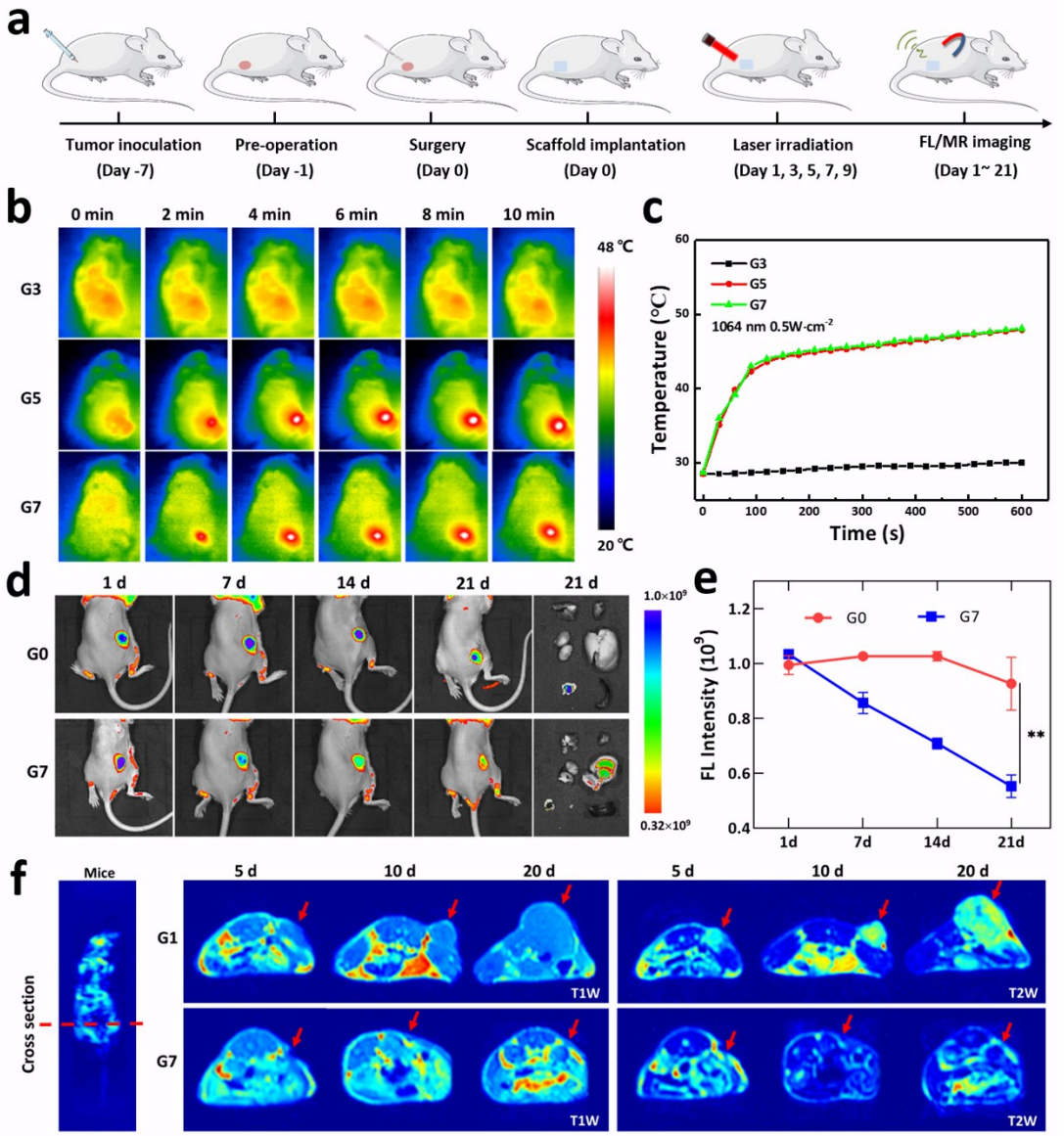

Figure 5. *In vivo* photothermal imaging and FL/MR imaging. (a) Treatment schedule of operation, scaffold implantation, and post-treatment. (b, c) *In vivo* photothermal imaging under NIR-II laser irradiation (0.5 W·cm^{-2}) and temperature recording in real-time. (d, e) *In vivo* FL imaging and FL intensity of G0 and G7 samples at 1, 7, 14 and 21 days. (f) *In vivo* MR imaging of G1 and G7 samples at 5, 10 and 20 days. (n = 5).

3.8. In vivo prevention of postoperative cancer recurrence

Encouraged by the efficient inhibition on 4T1 cells *in vitro*, we also attempted to verify the inhibition effect of composite scaffolds *in vivo*. As shown in **Figure 6a**, the surgical and implantation process consists of anesthetization, exposure of tumor, removal of the tumor, scaffold implantation, and suture. During the *in vivo* study, the tumor volume was periodically monitored by digital calipers every three days for a duration of three weeks. **Figure 6b**, **c** shows the average recurrent tumor volume on day 21 was 2459 mm^3 (G1), 2083 mm^3 (G2) and 1545 mm^3 (G3), and the recurrent tumor weight was approximately 2.08 g, 1.98 g, and 1.94 g, respectively, indicating that post-operative tumor recurrence is evident after these treatments. However, the average tumor volume on day 21 were much smaller at 1209 mm^3 (G4), 695 mm^3 (G5), 662 mm^3 (G6) and 13 mm^3 (G7) and the tumor weight much lower at 1.57 g, 1.16 g, 1.00 g and 0.20 g, respectively. Notably, improved antitumor effect was achieved when tumor-bearing mice were treated with GNR/DOX/PCF@ZIF-8+Laser scaffolds with 90.3% reduction of tumor weight presented at day 21; the corresponding tumor photographs are shown in **Figure 6d**. These results further show that the composite scaffold of G7 can effectively inhibit tumor recurrence and the survival rate of G7 mice was 100% at 21 days (**Figure 6e**). Meanwhile, there was no significant difference in body weight of mice among all groups after treatment, indicating low systemic toxicity of our GNR/DOX/PCF@ZIF-8 scaffolds (**Figure 6f**).

To confirm the anti-recurrence effect of the tumors, we performed histological (hematoxylin/eosin (H&E) staining, *in situ* terminal deoxynucleotide transferase-

mediated UTP terminal labeling (TUNEL) staining) and immunohistochemical Ki67 staining on different groups of tumor tissues (**Figure 6g**). As depicted in the H&E staining images, almost no tumor cell apoptosis was observed in the G1, G2, and G3 samples. Different degrees of tumor cell apoptosis were observed in G4, G5, and G6 samples, indicating that a single photothermal agent or laser irradiation can induce tumor cell apoptosis, but not completely. In contrast, from tumor tissue sections in the G7 samples, more fragmented nuclei and lighter cytoplasmic staining were observed, suggesting that the tumor tissue treated by photothermal-chemotherapy had undergone degenerative changes. Similarly, from the TUNEL staining images, most apoptotic tumor cells in G7 samples were stained with deoxy-RNA terminal transferase, suggesting endogenous DNA breakage in tumor cells. From the Ki67 staining images, the lowest positive rate of Ki67 and the largest area of blue-stained cells were observed in the G7 samples, confirming that most tumor cells were in the non-proliferative state thanks to the combination of photothermal-chemotherapy. The expression of heat shock protein 70 (HSP70) was analyzed to further explore the synergistic anti-cancer mechanism of photothermal and chemotherapy.[69] HSP70 is synthesized to cope with external heat stress and avoid cell damage by heat. Compared with the other groups without laser treatment, HSP70 expression of G5 and G7 samples with laser treatment was significantly increased, indicating that PTT-induced hyperthermia could successfully inhibit tumor growth. This provides further evidence that local photothermal combined with chemotherapy can significantly induce tumor cell apoptosis and inhibit tumor recurrence.

Finally, metastatic formation in the lungs of BALB/c mice was evaluated, as the lung is a priority site for metastases from advanced breast cancer. The lung specimens of each group were examined by macroscopic and microscopic examination after H&E staining. The H&E staining of the heart, liver, spleen, and kidney on day 21 was also conducted (**Figure S7**). From the H&E staining images, the composite scaffold implantation groups showed no obvious toxicity to major organs, and there are no degenerative changes were observed. As shown in **Figure 6h**, the necropsy showed that GNR/DOX/PCF@ZIF-8+Laser scaffolds significantly reduced the number of pulmonary metastatic tumor nodules (G7, 1 nodule), while large numbers of nodules were observed in G1, G2, G3, and other groups (G1, 22 nodules; G2, 21 nodules; G3, 18 nodules; G4, 11 nodules; G5, 9 nodules; G6, 5 nodules) (**Figure 6i**). The decrease in the number of metastatic tumor nodules after local treatment may reflect the inhibition of the regeneration of the primary tumor site and the corresponding survival data. In summary, these results indicate that this core-shell phase-change fibrous scaffold combined with laser irradiation can significantly inhibit tumor growth and metastases *in vivo*.

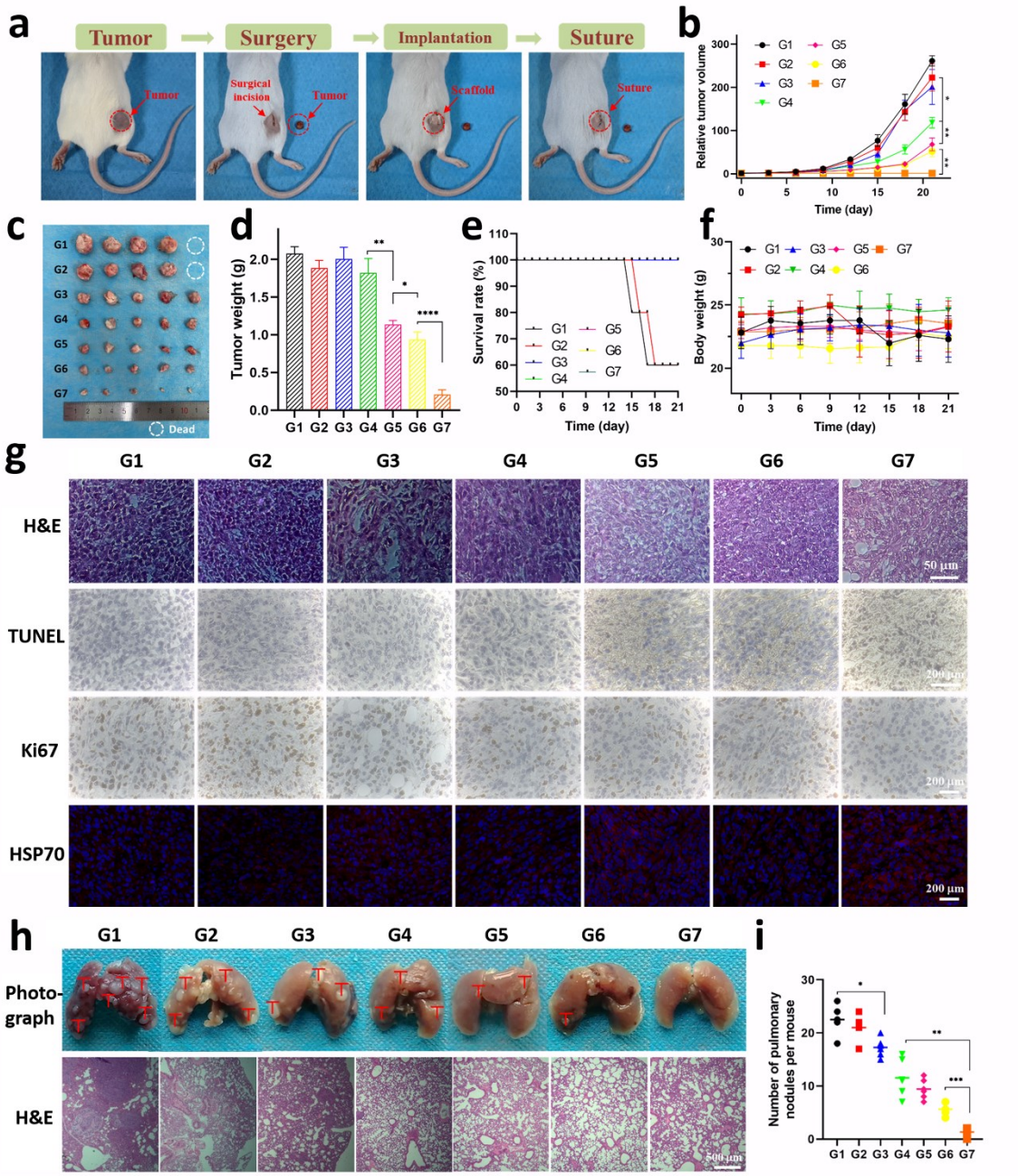

Figure 6. *In vivo* anti-tumor recurrence and metastasis effect. (a) The surgical and implantation process consists of anesthetization, exposure of tumor, implantation, and suture. (b) Volume changes of recurrent tumor within 21 days and composite scaffolds implantation. (c) Photographic images of mice and excised tumors. (d) Tumor weight. (e) The survival rate of mice within 21 days. (f) Bodyweight. (g) H&E staining, TUNEL staining, Ki67 staining, HSP70 expression of tumor tissue sections. (h) Photographic images (pulmonary nodules are marked by red T) and H&E staining images of excised lungs at day 21. (i) Statistics of pulmonary nodules. (n = 5).

4. Conclusion

In summary, we have successfully developed a programmable-response phase-change fibrous triggerable scaffold combining photothermal and chemotherapy for inhibiting post-operative recurrence and metastasis of breast cancer. The PCF@ZIF-8 scaffold with optimal core-shell and phase transition capability was successfully fabricated via electrospinning and post-treatment. The GNR/DOX co-loaded PCF@ZIF-8 scaffold exerted outstanding photothermal performance and drug release behavior with programmable sensitivity, which accelerated DOX release in an acidic tumor microenvironment and under NIR-II laser irradiation. Both *in vitro* and *in vivo* experimental results confirmed that the GNR/DOX/PCF@ZIF-8 scaffold significantly eliminates residual tumor cells from locally treated tumors with a tumor ablation rate of approximately 90.3% without significant damage to major organs. Thus, this new type of phase-change fibrous scaffold offers a promising alternative for post-operative photothermal-chemotherapy. PCF-based scaffolds also show promising potential in local drug release and temperature-regulation for avoiding damage to adjacent tissues.

Acknowledgment

The authors thank the financial support from National Key R&D Program of China (No. 2017YFC11050003), National Natural Science Foundation of China (No. 21807046), Guangdong Project (No. 2016ZT06C322), National Natural Science Foundation of Guangdong (No. 2020A151501744), Science and Technology Program of Guangzhou (No. 201907010032 and 202102020759), Fundamental Research Funds

for the Central Universities (No. 2020ZYGXZR064) and Guangdong University Student Science and Technology Innovation Cultivation Special Fund Project (No. pdjh2020a0032).

References

(1) Sung, H.; Ferlay, J.; Siegel, R. L.; Laversanne, M.; Soerjomataram, I.; Jemal, A.; Bray, F. Global Cancer Statistics 2020: GLOBOCAN Estimates of Incidence and Mortality Worldwide for 36 Cancers in 185 Countries, *Ca-Cancer J. Clin.* **2021**, *71*, 209-249.
(2) Bianchini, G.; Balko, J. M.; Mayer, I. A.; Sanders, M. E.; Gianni, L. Triple-negative Breast Cancer: Challenges and Opportunities of A Heterogeneous Disease, *Nat. Rev. Clin. Oncol.* **2016**, *13*, 674-690.
(3) Haffty, B. G.; Yang, Q.; Reiss, M.; Kearney, T.; Higgins, S. A.; Weidhaas, J.; Harris, L.; Hait, W.; Toppmeyer, D. Locoregional Relapse and Distant Metastasis in Conservatively Managed Triple Negative Early-stage Breast Cancer, *J. Clin. Oncol.* **2006**, *24*, 5652-5657.
(4) Luo, L.; Xu, F.; Peng, H.; Luo, Y.; Tian, X.; Battaglia, G.; Zhang, H.; Gong, Q.; Gu, Z.; Luo, K. Stimuli-responsive Polymeric Prodrug-based Nanomedicine Delivering Nifuroxazide and Doxorubicin Against Primary Breast Cancer and Pulmonary Metastasis, *J. Control. Release* **2020**, *318*, 124-135.
(5) Melamed, J. R.; Edelstein, R. S.; Day, E. S. Elucidating The Fundamental Mechanisms of Cell Death Triggered by Photothermal Therapy, *ACS Nano* **2015**, *9*, 6-11.
(6) Alkilany, A. M.; Thompson, L. B.; Boulos, S. P.; Sisco, P. N.; Murphy, C. J. Gold Nanorods: Their Potential for Photothermal Therapeutics and Drug Delivery,Tempered by the Complexity of Their Biological Interactions, *Adv. Drug. Deli. Rev.* **2012**, *64*, 190-199.
(7) Bao, Y.W.; Hua, X.W.; Li, Y.H.; Jia, H.R.; Wu, F.G. Hyperthemia-promoted Cytosolic and Nuclear Delivery of Copper/carbon Quantum Dot-crosslinked Nanosheets: Multimodal Imaging-guided Photothermal Cancer Therapy. *ACS Appl. Mater. Inter.* **2018**, *10*, 1544-1555.
(8) Dai, J. M.; Luo, Y.; Nie, D.; Jin, J. H.; Yang, S. L.; Li, G.; Yang, Y. M.; Zhang, W. pH/Photothermal Dual-responsive Drug Delivery and Synergistic Chemo-photothermal Therapy by Novel Porous Carbon Nanofibers, *Chem. Eng. J.* **2020**, *397*, 125402.
(9) Zheng, R.; Wang, S.; Tian, Y.; Jiang, X.; Fu, D.; Shen, S.; Yang, W. Polydopamine-coated Magnetic Composite Particles with An Enhanced Photothermal Effect. *ACS Appl. Mater. Inter.* **2015,** *7*, 15876-15884.

(10) He, S. Q.; Song, J.; Qu, J. L.; Cheng, Z. Crucial Breakthrough of Second Near-infrared Biological Window Fluorophores: Design and Synthesis toward Multimodal Imaging and Theranostics, *Chem. Soc. Rev.* **2018**, *47*, 4258-4278.
(11) Deng, X. R.; Liang, S.; Cai, X. C.; Huang, S. S.; Cheng, Z. Y.; Shi, Y. S.; Pang, M. L.; Ma, P. A.; Lin, J. Yolk-shell Structured Au Nanostar@metal-organic Framework for Synergistic Chemo-photothermal Therapy in The Second Near-infrared Window, *Nano Lett.* **2019**, *19*, 6772-6780.
(12) Talebian, S.; Foroughi, J.; Wade, S. J.; Vine, K. L.; Dolatshahi-Pirouz, A.; Mehrali, M.; Conde, J.; Wallace, G. G. Biopolymers for Antitumor Implantable Drug Delivery Systems: Recent Advances and Future Outlook, *Adv. Mater.* **2018**, *30*, 1706665.
(13) Xi, Y.; Ge, J.; Wang, M.; Chen, M.; Niu, W.; Cheng, W.; Xue, Y.; Lin, C.; Lei, B. Bioactive Anti-inflammatory, Antibacterial, Antioxidative Silicon-based Nanofibrous Dressing Enables Cutaneous Tumor Photothermo-chemo Therapy and Infection-induced Wound Healing, *ACS Nano* **2020**, *14*, 2904-2916.
(14) Agarwal, S.; Greiner, A.; Wendorff, J. H. Functional Materials by Electrospinning of Polymers, *Prog. Polym. Sci.* **2013**, *38*, 963-991.
(15) Wang, X.; Ding, B.; Sun, G.; Wang, M.; Yu, J. Electro-spinning/netting: A strategy for the Fabrication of Three-dimensional Polymer Nano-fiber/nets, *Prog. Mater. Sci.* **2013***, 58*, 1173-1243.
(16) Chen, S.; Li, R.; Li, X.; Xie, J. Electrospinning: An Enabling Nanotechnology Platform for Drug Delivery and Regenerative Medicine, *Adv. Drug. Deli. Rev.* **2018**, *132*, 188-213.
(17) Yang, G.; Li, X.; He, Y.; Ma, J.; Ni, G.; Zhou, S. From Nano to Micro to Macro: Electrospun Hierarchically Structured Polymeric Fibers for Biomedical Applications, *Prog. Polym. Sci.* **2018**, *81*, 80-113.
(18) Ding, J.; Zhang, J.; Li, J.; Li, D.; Xiao, C.; Xiao, H.; Yang, H.; Zhuang, X.; Chen, X. Electrospun Polymer Biomaterials, *Prog. Polym. Sci.* **2019**, *90*, 1-34.
(19) Chen, L.; Wang, S.; Yu, Q.; Topham, P. D.; Chen, C.; Wang, L. G. A Comprehensive Review of Electrospinning Block Copolymers, *Soft Matter* **2019**, *15*, 2490-2510.
(20) Jia, Y. F.; Yang, C. Y.; Chen, X. Y.; Xue, W. Q.; Hutchins-Crawford, H. J.; Yu, Q. Q.; Topham, P. D.; Wang, L. G. A Review on Electrospun Magnetic Nanomaterials: Methods, Properties and Applications, *J. Mater. Chem. C* **2021**, *9*, 9042-9082.
(21) Wang, X.; Ding, B.; Li, B. Biomimetic Electrospun Nanofibrous Structures for Tissue Engineering, *Mater. Today* **2013**, *16*, 229-241.
(22) Ding, Y.; Li, W.; Zhang, F.; Liu, Z.; Ezazi, N. Z.; Liu, D.; Santos, H. A. Electrospun Fibrous Architectures for Drug Delivery, Tissue Engineering and Cancer Therapy, *Adv. Funct. Mater.* **2019**, *29*, 1802852.
(23) Shao, J.; Xie, H.; Wang, H.; Zhou, W.; Luo, Q.; Yu, X.F.; Chu, P.K. 2D Material-based Nanofibrous Membrane for Photothermal Cancer Therapy, *ACS Appl. Mater. Inter.* **2018**, *10*, 1155-1163.
(24) Li, W.; Yu, Q.; Yao, H.; Zhu, Y.; Topham, P. D.; Yue, K.; Ren, L.; Wang, L. Superhydrophobic Hierarchical Fiber/bead Composite Membranes for Efficient Treatment of Burns, *Acta Biomater.* **2019**, *92*, 60-70.

(25) Chen, L.; Yu, Q.; Jia, Y.; Xu, M.; Wang, Y.; Wang, J.; Wen, T.; Wang, L. Micro-and-nanometer Topological Gradient of Block Copolymer Fibrous Scaffolds towards Region-specific Cell Regulation, *J. Collid. Interf. Sci.* **2022**, *66*, 248-260.
(26) Zhao, J.; Cui, W. Functional Electrospun Fibers for Local Therapy of Cancer, *Adv. Fiber. Mater.* **2020**, *2*, 229-245.
(27) Luo, H.; Kong, L.; Zhang, F.; Huang, C.; Chen, J.; Zhang, H.; Yu, H.; Zheng, S.; Xu, H.; Zhang, Y.; Deng, L.; Chen, G.; Santos, H. A.; Cui, W. Light-controlled Nanosystem with Size-flexibility Improves Targeted Retention for Tumor Suppression, *Adv. Funct. Mater.* **2021**, *31*, 2101262.
(28) Li, X.; Xu, F.; He, Y.; Li, Y.; Hou, J.; Yang, G.; Zhou, S. A Hierarchical Structured Ultrafine Fiber Device for Preventing Postoperative Recurrence and Metastasis of Breast Cancer, *Adv. Funct. Mater.* **2020**, *30*, 2004851.
(29) Xiao, Y.; Fan, Y.; Tu, W.; Ning, Y.; Zhu, M.; Liu, Y.; Shi, X. Multifunctional PLGA Microfibrous Rings Enable MR Imaging-guided Tumor Chemotherapy and Metastasis Inhibition through Prevention of Circulating Tumor Cell Shedding, *Nano Today* **2021**, *38* 101123.
(30) Zhang, Z.; Liu, S.; Xiong, H.; Jing, X.; Xie, Z.; Chen, X.; Huang, Y. Electrospun PLA/MWCNTs Composite Nanofibers for Combined Chemo- and Photothermal Therapy, *Acta Biomater.* **2015**, *26*, 115-123.
(31) Bhattarai, D. P.; Tiwari, A. P.; Maharjan, B.; Tumurbaatar, B.; Park, C. H.; Kim, C. S. Sacrificial Template-based Synthetic Approach of Polypyrrole Hollow Fibers for Photothermal Therapy, *J. Colloid. Interf. Sci.* **2019**, *534*, 447-458.
(32) Park, J. H.; Seo, H.; Kim, D. I.; Choi, J. H.; Son, J. H.; Kim, J.; Moon, G. D.; Hyun, D. C. Gold Nanocage-incorporated Poly(epsilon-caprolactone) (PCL) Fibers for Chemophotothermal Synergistic Cancer Therapy, *Pharmaceutics* **2019**, *11*, 60-74.
(33) Tiwari, A. P.; Bhattarai, D. P.; Maharjan, B.; Ko, S. W.; Kim, H. Y.; Park, C. H.; Kim, C. S. Polydopamine-based Implantable Multifunctional Nanocarpet for Highly Efficient Photothermalchemo Therapy, *Sci. Rep.* **2019**, *9*, 2943-2956.
(34) Choi, S. W.; Zhang, Y.; Xia, Y. N. A Temperature-sensitive Drug Release System Based on Phase-change Baterials, *Angew. Chem. Int. Edit.* **2010**, *49*, 7904-7908.
(35) Yuan, Y. P.; Zhang, N.; Tao, W. Q.; Cao, X. L.; He, Y. L. Fatty Acids as Phase Change Materials: A review, *Renew. Sus. Energ. Rev.* **2014**, *29*, 482-498.
(36) Harish, S.; Orejon, D.; Takata, Y.; Kohno, M. Thermal Conductivity Enhancement of Lauric Acid Phase Change Nanocomposite with Graphene Nanoplatelets, *Appl. Therm. Eng.* **2015**, *80*, 205-211.
(37) Qiu, J. C.; Huo, D.; Xue, J. J.; Zhu, G. H.; Liu, H.; Xia, Y. N. Encapsulation of A Phase-change Material in Nanocapsules with A Well-defined Hole in The Wall for The Controlled Release of Drugs, *Angew. Chem. Int. Edit.* **2019**, *58*, 10606-10611.
(38) Li, Q.; Sun, L. H.; Hou, M. M.; Chen, Q. B.; Yang, R. H.; Zhang, L.; Xu, Z. G.; Kang, Y. J.; Xue, P. Phase-change Material Packaged within Hollow Copper Sulfide Nanoparticles Carrying Doxorubicin and Chlorin e6 for Fluorescence-guided Trimodal Therapy of Cancer, *ACS Appl. Mater. Inter.* **2019**, *11*, 417-429.

(39) Xue, J. J.; Zhu, C. L.; Li, J. H.; Li, H. X.; Xia, Y. N. Integration of Phase-change Materials with Electrospun Fibers for Promoting Neurite Outgrowth under Controlled Release, *Adv. Funct. Mater.* **2018**, *28*, 1705563.
(40) Poudel, B. K.; Soe, Z. C.; Ruttala, H. B.; Gupta, B.; Ramasamy, T.; Thapa, R. K.; Gautam, M.; Ou, W. Q.; Nguyen, H. T.; Jeong, J. H.; Jin, S. G.; Choi, H. G.; Yong, C. S.; Kim, J. O. In Situ Fabrication of Mesoporous Silica-coated Silver-gold Hollow Nanoshell for Remotely Controllable Chemo-photothermal Therapy via Phase-change Molecule as Gatekeepers, *Int. J. Pharmaceut.* **2018**, *548*, 92-103.
(41) Hyun, D. C.; Lu, P.; Choi, S. I.; Jeong, U.; Xia, Y. N. Microscale Polymer Bottles Corked with A Phase-change Material for Temperature-controlled Release, *Angew. Chem. Int. Edit.* **2013**, *52*, 10468-10471.
(42) Wu, Y.; Chen, C. Z.; Jia, Y. F.; Wu, J.; Huang, Y.; Wang, L. G. Review on Electrospun Ultrafine Phase Change Fibers (PCFs) for Thermal Energy Storage, *Appl. Energ.* **2018**, *210*, 167-181.
(43) Qiu, J.; Huo, D.; Xia, Y. Phase-Change Materials for Controlled Release and Related Applications, *Adv. Mater.* **2020**, *32*, 2000660.
(44) Oro, E.; de Gracia, A.; Castell, A.; Farid, M. M.; Cabeza, L. F. Review on Phase Change Materials (PCMs) for Cold Thermal Energy Storage Applications, *Appl. Energ.* **2012**, *99*, 513-533.
(45) Hyun, D. C.; Levinson, N. S.; Jeong, U.; Xia, Y. A. Emerging Applications of Phase-change Materials (PCMs): Teaching An Old Dog New Tricks, *Angew. Chem. Int. Edit.* **2014**, *53*, 3780-3795.
(46) Chen, C. Z.; Wang, L. G.; Huang, Y. Electrospun Phase Change Fibers Based on Polyethylene glycol/Cellulose Acetate Blends, *Appl. Energ.* **2011**, *88*, 3133-3139.
(47) Chen, C. Z.; Chen, J.; Jia, Y. F.; Topham, P. D.; Wang, L. G. Binary Shape-stabilized Phase Change Materials Based on Poly(ethylene glycol)/Polyurethane Composite with Dual-phase Transition, *J. Mater. Sci.* **2018**, *53*, 16539-16556.
(48) Chen, C. Z.; Wang, L. G.; Huang, Y. Morphology and Thermal Properties of Electrospun Fatty Acids/Polyethylene Terephthalate Composite Fibers as Novel Form-stable Phase Change Materials, *Sol. Energ. Mater. Sol. C* **2008**, *92*, 1382-1387.
(49) Chen, C. Z.; Wang, L. G.; Huang, Y. Ultrafine Electrospun Fibers Based on Stearyl Stearate/Polyethylene Terephthalate Composite as Form Stable Phase Change Materials, *Chem. Eng. J.* **2009**, *150*, 269-274.
(50) Wu, M. X.; Yang, Y. W. Metal-organic Framework (MOF)-based Drug/Cargo Delivery and Cancer Therapy, *Adv. Mater.* **2017**, *29*, 1606134.
(51) Yuan, Y.; Zhang, N.; Tao, W.; Cao, X.; He, Y. Fatty Acids as Phase Change Materials: A Review, *Renew. Sus. Energ. Rev.* **2014**, *29*, 482-498.
(52) Aliko, K.; Aldakhlalla, M. B.; Leslie, L. J.; Worthington, T.; Topham, P. D.; Theodosiou, E. Poly(butylene succinate) Fibrous Dressings Containing Natural Antimicrobial Agents, *J. Ind. Text.* **2021**, DOI: 10.1177/152808372098720920.
(53) Bye, F. J.; Wang, L.; Bullock, A. J.; Blackwood, K. A.; Ryan, A. J.; MacNeil, S. Postproduction Processing of Electrospun Fibres for Tissue Engineering, *Jove-J. Vis. Exp.* **2012**, *66*, e4172.

(54) Chen, H.; Shao, L.; Ming, T.; Sun, Z.; Zhao, C.; Yang, B.; Wang, J. Understanding The Photothermal Conversion Efficiency of Gold Nanocrystals, *Small*. **2010**, 6, 2272-2280.
(55) Jin, Z. J. About The Evaluation of Drug Combination, *Acta Pharmacol. Sin.* **2004**, *25*, 146-147.
(56) Liu, W.; Zhang, H.; Zhang, W.; Wang, M.; Li, J.; Zhang, Y.; Li, H. Surface Modification of A Polylactic Acid Nanofiber Membrane by Zeolitic Imidazolate Framework-8 from Secondary Growth for Drug Delivery, *J. Mater. Sci.* **2020**, *55*, 15275-15287.
(57) Chen, C. Z.; Wang, L. G.; Huang, Y. A Novel Shape-stabilized PCM: Electrospun Ultrafine Fibers Based on Lauric Acid/Polyethylene Terephthalate Composite, *Mater. Lett.* **2008,** *62*, 3515-3517.
(58) Cai, Y. B.; Ke, H. Z.; Dong, J.; Wei, Q. F.; Lin, J. L.; Zhao, Y.; Song, L.; Hu, Y. A.; Huang, F. L.; Gao, W. D.; Fong, H. Effects of Nano-SiO_2 on Morphology, Thermal Energy Storage, Thermal Stability, and Combustion Properties of Electrospun Lauric Acid/PET Ultrafine Composite Fibers as Form-stable Phase Change Materials, *Appl. Energ.* **2011**, *88*, 2106-2112.
(59) Zhen, X.; Xie, C.; Pu, K. Temperature-correlated Afterglow of A Semiconducting Polymer Nanococktail for Imaging-guided Photothermal Therapy, *Angew. Chem. Int. Edit.* **2018,** *57*, 3938-3942.
(60) Zhu, X.; Feng, W.; Chang, J.; Tan, Y.-W.; Li, J.; Chen, M.; Sun, Y.; Li, F. Temperature-feedback Upconversion Nanocomposite for Accurate Photothermal Therapy at Facile Temperature, *Nat. Commun.* **2016**, *7*, 10437.
(61) Vigderman, L.; Zubarev, E. R. High-yield Synthesis of Gold Nanorods with Longitudinal SPR Peak Greater Than 1200 nm Using Hydroquinone as A Reducing Agent, *Chem. Mater.* **2013**, *25*, 1450-1457.
(62) Tsai, M. F.; Chang, S. H. G.; Cheng, F. Y.; Shanmugam, V.; Cheng, Y. S.; Su, C. H.; Yeh, C. S. Au Nanorod Design as Light-absorber in The First and Second Biological Near-infrared Windows for In Vivo Photothermal Therapy, *ACS Nano.* **2013**, *7*, 5330-5342.
(63) Bi, C. X.; Chen, J.; Chen, Y.; Song, Y. H.; Li, A. R.; Li, S. Z.; Mao, Z. W.; Gao, C. Y.; Wang, D. Y.; Mohwald, H.; Xia, H. B. Realizing A Record Photothermal Conversion Efficiency of Spiky Gold Nanoparticles in The Second Near-infrared Window by Structure-based Rational Design, *Chem. Mater.* **2018**, *30*, 2709-2718.
(64) Wang, Q. S.; Wang, H.; Yang, Y.; Jin, L. H.; Liu, Y.; Wang, Y.; Yan, X. Y.; Xu, J.; Gao, R. Q.; Lei, P. P.; Zhu, J. J.; Wang, Y. H.; Song, S. Y.; Zhang, H. J. Plasmonic Pt Superstructures with Boosted Bear-infrared Absorption and Photothermal Conversion Efficiency in The Second Biowindow for Cancer Therapy, *Adv. Mater.* **2019**, *31*, 1904836.
(65) Cao, W.; He, Y.; Zhu, R.; He, Y.; Hao, Z.; Zhao, Q.; He, H.; Wang, S.; Li, C.; Gao, D. NIR Light Triggered Size Variable "Remote-controlled Cluster Bomb" for Deep Penetration and Tumor Therapy, *Chem. Eng. J.* **2019**, *375*, 122080.
(66) Liu, J.; Chen, Q.; Feng, L.; Liu, Z. Nanomedicine for Tumor Microenvironment Modulation and Cancer Treatment Enhancement, *Nano Today.* **2018**, *21*, 55-73.

(67) Feng, J.; Xu, Z.; Dong, P.; Yu, W. Q.; Liu, F.; Jiang, Q. Y.; Wang, F.; Liu, X. Q. Stimuli-responsive Multifunctional Metal-organic Framework Nanoparticles for Enhanced Chemo-photothermal Therapy, *J. Mater. Chem. B.* **2019**, *7,* 994-1004.
(68) Van Du, N.; Min, H.-K.; Kim, D.-H.; Kim, C.-S.; Han, J.; Park, J.-O.; Choi, E. Macrophage-mediated Delivery of Multifunctional Nanotherapeutics for Synergistic Chemo-photothermal Therapy of Solid Tumors, *ACS Appl. Mater. Inter.* **2020**, *12,* 10130-10141.
(69) Vankayala, R.; Lin, C. C.; Kalluru, P.; Chiang, C. S.; Hwang, K. C. Gold Nanoshells-mediated Bimodal Photodynamic and Photothermal Cancer Treatment using Ultra-low Doses of Near Infra-red Light, *Biomaterials.* **2014**, *35,* 5527-5538.